Seismic evidence for a weakened thick crust at the Beaufort Sea continental margin

C. Estève[1], Y. Liu[1], I. Koulakov[2], A. J. Schaeffer[3], and P. Audet[4]

[1]Department of Earth and Planetary Sciences, McGill University, Montreal, Quebec, Canada
[2]Trofimuk Institute of Petroleum Geology and Geophysics, SB RAS, Novosibirsk, Russia
[3]Geological Survey of Canada, Pacific Division, Natural Resources Canada, Sidney, British Columbia, Canada
[4]Department of Earth and Environmental Sciences, University of Ottawa, Ottawa, Ontario, Canada

Key Points:

- We present new seismic velocity models (V_P, V_S and V_P/V_S) of the Beaufort Sea continental margin
- We find localized thickened crust below the Beaufort Sea continental margin of northern Yukon
- Deformation is controlled by lateral variation in crustal strength attributed to different crustal compositions in the region

Corresponding author: Clément Estève, `clement.esteve@mail.mcgill.ca`

Abstract

The Canadian Beaufort Sea continental margin of northwestern Canada is a Cenozoic convergent margin, potentially representing a rare case of incipient subduction. Here, we produce P- and S-wave seismic velocity models of the crust and the uppermost mantle using recordings from regional earthquakes. Our models reveal a northwest-dipping very low-velocity anomaly within the crust (δV up to -15%) beneath the Romanzof Uplift. We interpret this low-velocity feature to correspond to a weaker and thicker crust due to shortening and stacking of igneous and sedimentary rocks. The co-location of the thickened crust and lack of present-day seismicity indicates that north-south compression is accommodated by slow, aseismic deformation in the narrow margin beneath the Romanzof Uplift or more broadly offshore. Neither interpretation requires a subduction initiation process.

Plain Language Summary

The Canadian Beaufort Sea continental margin of northwestern Canada may represent a unique location in the world where we observe a newly forming convergent margin, potentially representing a rare case of incipient subduction. We develop 3-D seismic velocity models of the region from the crust to the uppermost mantle using regional earthquake recordings. The velocity models reveal a low-velocity zone within the crust beneath the Beaufort Sea continental margin of the Yukon north slope. Seismic velocities in the crust predominantly depend on rock composition. Therefore, we suggest that variations in rock compositions influence the observed deformation processes and that crustal thickening occurs locally in the area. The observation of the thickened crust and lack of seismicity in the area suggest that deformation could be accommodated aseismically across the narrow margin or more broadly offshore. Neither interpretation requires a subduction initiation mechanism.

1 Introduction

The Beaufort Sea continental margin (BSCM - Figure 1) has recorded several episodes of deformation through geological time. In particular, the Romanzof Uplift (Figure 1) is associated with compressional deformation and tectonic uplift from late Early Devonian to earlier Middle Devonian

(Lane, 2007). This compressive deformation generated folds and north-oriented thrust faults and was associated with Late Devonian granitic plutons (Lane, 2007). From Late Cretaceous to Late Miocene time, several pulses of orogenic deformation occurred. In particular, the arcuate Beaufort fold-and-thrust belt formed onshore and offshore within the BSCM (Figure 1) during Paleocene time and continued to middle Eocene (Lane, 2002). The formation of the fold-and-thrust belt is related to the interaction of several geological events: 1) east-west shortening of northern Yukon between Arctic Alaska and the North American craton caused by the opening of the Atlantic Ocean; 2) subduction of the Kula and Pacific plates beneath North America; and 3) northward escape of deforming supracrustal rocks into the Beaufort Sea (Lane, 1998) due to buttressing of the rigid North American craton beneath the Richardson Mountains, which define the current eastern limit of the Cordillera (Lane, 1998; Saltus & Hudson, 2007; Estève et al., 2020).

Seismicity near the BSCM is distributed across 3 regions: the Richardson Mountains, northeastern Alaska and beneath the Beaufort Sea (Figure 1). Focal mechanisms for earthquakes in the Richardson Mountains suggest right-lateral strike slip motion along a north-south trending plane, consistent with the mapped surface faults in the region (Figure 1; Cassidy et al., 2005). Here the largest recorded earthquakes occurred in May and June 1940 (M_S 6.2 and 6.5, respectively; Cassidy & Bent, 1993). A northeast-southwest left-lateral diffuse deformation zone is also observed around the Canning River in the northeastern corner of Alaska (Hyndman et al., 2005). In August 2018, the largest earthquakes recorded in northern Alaska (M_W 6.0 and M_W 6.4) occurred in the northeastern Brooks Range, highlighting the potential for damaging earthquakes on previously unknown faults (Gaudreau et al., 2019). Further north, a cluster of seismicity is observed within the Beaufort Sea but its origin remains poorly constrained. This seismic cluster produces on average one moderate earthquake ($M > 4$) per year, characterized by a subcrustal focal depth (from 18 to 40 km depth; Audet & Ma, 2018). The largest earthquake ($M > 6$) in the Beaufort Sea occurred in 1920, suggesting that the region is subject to infrequent but large earthquakes (Hasegawa et al., 1979). The few focal mechanisms available show normal and strike-slip faulting but these are poorly constrained (Hasegawa et al., 1979; Hyndman et al., 2005).

The BSCM currently accommodates slow ($\sim$ 2 mm/yr) tectonic deformation, interpreted to reflect convergence of the Beaufort Sea lithosphere with the North American margin (Hyndman et al., 2005). Such convergence may be developing into a rare case of incipient subduction. However, earthquake distribution, relation to faults and subsurface structure in this region have so far been poorly constrained due to historical sparsity of seismic station coverage in northwestern Canada. In particular, no regional scale seismic imaging of the BSCM crustal and upper mantle structures is yet available to verify or refute the subduction initiation hypothesis. With the recent deployment of seismic networks such as the USArray Transportable Array (TA) across Alaska and Yukon Territory, seismic data are available from several seismograph stations in close proximity to the Beaufort Sea (Figure 1). Here we develop new three-dimensional seismic velocity models (V_P, V_S and V_P/V_S) of the crust and uppermost mantle using travel time data from regional earthquakes, and discuss their implications for the crustal material properties and tectonics of the Beaufort Sea continental margin.

2 Data and Method

We use seismic data from the Incorporated Research Institution for Seismology (IRIS) for 27 temporary and permanent seismic stations across northwestern Canada and northeastern Alaska (Figure 1) to extract 3-component seismograms of 1,080 regional earthquakes with $M_{\mathrm{W}} \geq 1.0$ that occurred from November 2012 to August 2021. We detrend, demean, taper and apply a Butterworth band-pass filter with a 2-15 Hz band range in order to suppress the high-frequency noise and correctly determine P and S phases for each seismogram. We visually inspect seismograms and manually pick clear P- and S-wave arrivals. We further cull this data set based on two criteria : 1) we discard earthquakes with less than 10 P- and S-wave picks; and 2) we remove P- or S-wave arrival times with residual values exceeding 1.7 s after re-locating the sources in the 1-D starting velocity model. This results in 13,470 and 13,329 P- and S-wave arrival times, respectively, from 925 events, as the input data set for the tomographic inversion (Figure S1).

We use the Local Tomography Software (LOTOS) to estimate the three-dimensional isotropic seismic velocity structure (Koulakov, 2009). LOTOS has been successfully applied to a variety of tectonic settings (*e.g.,* collision zones: Talebi et al. (2020); Medved et al. (2021), subduction zones: Foix et al. (2019), ocean-continent transition zone: El Khrepy et al. (2021) and paleo-rift system in eastern Canada: Onwuemeka et al. (2021)). Starting with a 1-D (i.e., layered) velocity model, the software calculates the travel times based on a reference table of initial event locations, and uses a grid search method to relocate all events (Koulakov & Sobolev, 2006). The earthquakes are then iteratively relocated using a 3-D bending ray tracing method (Um & Thurber, 1987) with subsequently updated 3-D velocity models at each iteration.

We construct the starting 1-D reference velocity model by calculating an average 1-D V_S model from the pseudo three-dimensional V_S model of Estève et al. (2021). Conversion of V_S to V_P is carried out using a regional average V_P/V_S calculated for the seismic stations in our study area (Audet et al., 2020). Then, we compute the average V_P and V_S values at specific depths, after running the full LOTOS inversion procedure once. These values are used as the new 1-D reference velocity model for the LOTOS inversion. After several iterations, we obtain the optimal reference model presented in Table S1. V_P and V_S in the starting 1-D reference velocity model are defined at several depth levels and linearly interpolated.

Parameterization of both P- and S-wave velocity models uses a set of nodes which depend on the ray density (Figures S4-S5). The spacing between nodes in the horizontal direction is 30 km in areas with sufficient ray density (*i.e.,* where the ray density normalized by the average ray density is greater than 0.1). In the vertical direction, the grid spacing also depends on the ray density, but it cannot be smaller than a predefined minimum value (10 km). Between the nodes, velocity anomalies are linearly interpolated. In order to reduce artifacts in the tomographic model due to the geometric node distribution with respect to azimuthal sampling of ray paths, we perform the LOTOS inversion using several grids with different grid orientations (0°, 22°, 45°, and 67°). Each grid orientation is constructed during the first iteration and is unchanged for the remaining iterations. After all the four sets of inversions are completed, we average the four 3-D velocity models into one final velocity model on a regular grid (Figure S2). This regular grid is 450 x 450 x 200 km (x, y and z) where each block is 30 x 30 x 10 km. Also, areas within the model space that are 100 km away from the nearest node are considered unresolved (value is set to 0).

P-wave and S-wave arrival times are simultaneously inverted for P and S-wave velocity anomalies and earthquake hypocenters (*dx, dy, dz and dt*) using an iterative LSQR algorithm (Paige & Saunders, 1982; van der Sluis & van der Vorst, 1987). We use smoothing and damping parameters of 1.5 and 4 for the P-wave model and 2 and 3 for the S-wave model. These values were selected by evaluating checkerboard tests and RMS time residuals. We used 5 iterations to derive the final velocity models, as RMS time residuals no longer significantly decrease for subsequent iterations (Figure S3). We obtained a variance reduction of 35% and 37% for P- and S-wave data sets.

3 Model Resolution

We assess the resolution of our velocity models using checkerboard tests, structural tests, odd/even test and ray coverage (Figures S4-S16). Checkerboard test models consist of an alternating pattern of fast and slow velocity anomalies whose amplitudes are ±7% of the background velocity. We created these tests for two different configurations, where each anomaly is either 70 x 70 x 40 km (Figures S7-S9) or 50 x 50 x 40 km (Figures S10-S12). The synthetic travel times are computed using 3-D ray tracing and the noise level is defined as 40% and 60% of values of real remnant residuals, to model the picking error in the initial P- and S-wave data sets, respectively. The variance reduction in P- and S-wave travel time residuals, after 5 iterations, is similar to the real data inversion for both P- and S-wave velocity models (i.e., 35% and 37%, respectively). After computing the synthetic data, we perform the full inversion procedure, including the earthquake relocations, to investigate which parts of the model are best resolved. This results in a synthetic inversion that adequately reflects real data processing (Koulakov, 2009). After the final iteration, the average lateral and vertical errors of the source relocations are 2.80 km and 5.01 km, respectively (Figure S17). The event relocation errors within the Beaufort Sea are higher due to the lack of station coverage (Figure S17). Longer raypaths accumulate more travel time anomalies and are characterized by greater residuals (Koulakov, 2009). Therefore, these events have smaller weights than shorter raypaths in the relocation algorithm.

We show results for the checkerboard tests with 50- and 70-km-scale anomalies in Figures S7 to S12. Recovered checkerboard models show a clear distinction in resolution between the continental and the oceanic regions of the study area (Figures S7-S12). Anomalies located beneath the Beaufort Sea are not retrieved between the surface and 50 km depth because of the lack of crossing rays. At greater depths, along transect U-U', the amplitude recovery is less than 50% and synthetic anomalies within the Beaufort Sea are affected by lateral and vertical smearing (Figures S7-S12). The amplitudes are most accurate across the continental region of the model and the recovery becomes better at intermediate depths (40-60 km) due to the increase in crossing raypaths. However, we note that anomalies are laterally and vertically smeared across northeastern Alaska. The checkerboard tests indicate that the seismic velocity models can resolve anomalies with lateral dimensions of 50 km beneath most of the continental region.

In addition, we assess the role of random noise in the data by performing an odd/even test, which consists of two independent inversions of data subsets with the odd and even index numbers of the earthquake sequence respectively. Differences between the derived results reflect the effect of random noise. Figure S16 shows the results of the odd/even test at 20 km depth for P- and S-wave models. The locations, shapes and amplitudes of the main anomalies are similar in the models, reflecting the robustness of the final solution. However, we note that the high-velocity anomaly located in the northeastern Brooks Range and features offshore within the Beaufort Sea derived from the odd and even subsets do not match, indicating the important role of random noise. Finally, we also perform synthetic structural tests to evaluate the reliability of recovered long-wavelength anomalies. We will introduce the details of the structural test in Section 4.2.

4 Results

4.1 Relocated seismicity and fault structures

Figure 2 shows the distribution of relocated seismicity. Overall, the relocated hypocentral depths are shallower compared to the initial depths with some exceptions (Figure 2B). For example, most of the events within the Beaufort Sea are re-located deeper than 40 km, although those relocations are highly uncertain, as discussed previously (Figures S6 and S17). We note that most relocated earthquakes occur within a depth range of 0 to 20 km depth, implying that the brittle-ductile transition zone occurs between 20 and 30 km depth where seismicity decreases rapidly (Figure 2B).

Figure 2C and 2D show a zoom-in on the final event locations around the Richardson Mountains and across northeastern Alaska. Relocated events appear to deepen from north to south within the Richardson Mountains. However, we note that some events are relatively shallow in the southernmost part of the Richardson Mountains. Furthermore, relocated events are aligned in a narrower belt oriented north-south on the eastern side of the Richardson Mountains. This north-south feature correlates well with mapped fault traces (Figures 1 and 2). In cross-section view, these relocated events define one or several steep west-dipping faults (Figure S24). Toward the northern Richardson Mountains, we observe a cluster of seismicity located within the inner region of the mountain range, which is separated from the linear feature previously mentioned

(Figure 2C). Focal mechanisms suggest slip on normal faults, which is consistent with the average northwest-southeast maximum horizontal stress orientation (Figure 1B). Also, we note the sharp seismicity cut-off between the BSCM and the northern end of the Richardson Mountains.

Around the Canning River, northeastern Alaska (Figure 2), earthquake epicenters are oriented northwest-southeast and are located at depths ranging from the surface to 20 km. Most of these earthquakes are aftershocks following the August 2018 Kaktovik mainshock (M_W 6.4). This northwest-southeast orientation of the earthquake epicenters appears to be consistent with the orientation of two right-lateral strike-slip fault segments running obliquely to the Sadlerochit Mountains (see Figure 1 for location). These fault segments may have contributed to the August 2018 Katkovik earthquake sequence (Gaudreau et al., 2019).

4.2 P- and S-wave velocity anomalies and V_P/V_S estimates

We present the distribution of P- and S-wave velocity anomalies as well as V_P/V_S values in map view at 20 km depth (Figure 3, top row) and along three profiles (Figure 3 - middle and bottom rows). We also show absolute P, S-wave velocities and V_P/V_S depth slices and transects (Figures S18, S19, S20 and S21). V_P/V_S values are derived from the division of absolute P- and S-wave velocities. Overall, we observe that the distribution of seismic velocity anomalies are similar between the P-wave and S-wave models.

At the broadest scale, our seismic velocity models reveal generally negative anomalies (with respect to the background mean) within the crust west of the Richardson Mountains. Positive anomalies are located in the Beaufort Sea and Proterozoic Canadian Shield to the north and east of the Richardson Mountains, respectively; however, we note that these areas are not well constrained because of the sparse data coverage (Figure S6). Positive anomalies in the Cordillera are found below the Old Crow Basin and the continental margin in northern Alaska. An intriguing feature of the velocity models is the very low-velocity anomaly ($max\ \delta V = -15\%$) in northernmost Yukon below the eastern part of the Romanzof uplift (Figure 1), which extends to $>$ 40 km depth beneath the BSCM (Figure 3). In the lower crust, along transects B-B' and C-C', this low-velocity zone dips toward the northwest, extending below the Moho depth model of Estève et al. (2021) underlying the Arctic coast. This dipping anomaly (which we label the Romanzof Uplift Anomaly - RUA) is a robust feature in our velocity models, as highlighted by synthetic structural tests (Figures S13-

S14-S15), and is not biased by the azimuthal coverage of ray paths (Figures S7-S12). Recovered structural models show that such long-wavelength low-velocity anomalies can be reliably resolved at this location (Figures S13-S14-S15).

V_P/V_S values range between 1.6 and 1.9 and the distribution does not appear to correlate spatially with the velocity anomaly distributions. V_P/V_S is lowest (~ 1.6) in the Yukon Flats of eastern Alaska, and highest ($\sim 1.8 - 1.9$) within a narrow zone (~ 100 km) along the Beaufort Sea margin, northwest of the lowest-velocity feature (Figure 3, transect B-B').

5 Discussion

In general, earthquake distribution correlates with negative velocity anomalies, except in the RUA in northern Yukon where the crust is aseismic but seismic velocities are lowest. In this region, Pliocene sedimentary strata overlie older (pre-Carboniferous) sedimentary and igneous rocks that are folded and thrust faulted (Lane & Dietrich, 1995). In the RUA, absolute P- and S-wave velocities at 20 km depth are approximately 6.1-6.5 km/s (Figure S18) and 3.6-3.7 km/s (Figure S19), respectively, which indicate felsic compositions such as quartz mica schist, felsic granulite, granite-granodiorite and/or diorite (Figure S22; Christensen & Mooney, 1995). The estimated V_P/V_S values of $1.70 - 1.78$ are also consistent with a bulk felsic composition (granite-granodiorite, gneiss, felsic-granulite, metagraywacke and/or phyllite; Christensen, 1996). East and west of the RUA, absolute P- and S-wave velocities are 6.6-7.0 km/s and 3.8-4.0 km/s, respectively, at 20 km depth, corresponding to a more mafic composition (Figures S22B and S22C). We note that Moho depth estimates (Audet et al., 2020) coincide with the ~ 7 km/s, P-wave velocity contour (Fig. S21), except beneath the Romanzof Uplift where this contour extends into the lithospheric mantle. We therefore interpret the RUA to represent locally thickened crust (~ 50 km depth Moho; Fig. 4). However, we note that a Moho depth estimate from receiver function data for the station TA.D28M (Figure 1), located within the footprint of the RUA, is 33.5 ± 1.6 km. This is shallower than the inferred base of the RUA at ~ 50 km depth, although there is evidence of heterogeneity and/or anisotropy in the receiver function data that may further reflect weak deformation fabrics within the crust (Audet et al., 2020).

The lower strength of felsic rocks compared to mafic rocks at similar P-T conditions (*e.g.,* Wilks & Carter, 1990) could explain the lack of seismicity in the RUA. In northern Yukon, sparse GPS data reveal a north-northeastward motion relative to the stable North America craton to the east (*e.g.*, Leonard et al., 2007; Mazzotti et al., 2008). If this northward motion is accommodated within a narrow continental margin, it may represent a zone of potential high strain rate. In this case, the lack of seismicity of the RUA would suggest strain is accommodated through aseismic creep occurring via plastic deformation in weak rocks. Alternatively, the lack of seismicity may imply that current deformation occurs offshore further north within the Beaufort fold-and-thrust belt, and that strain rates are simply too low for seismic deformation within the RUA. Within the offshore fold-and-thrust belt, geological evidence suggests that Paleocene to early Eocene deformation is the result of the northward propagation of thrusting and is associated with thin-skinned deformation mobilizing sedimentary cover (Lane & Dietrich, 1995; Lane, 1998), which may lead to subduction initiation (Hyndman et al., 2005).

Figure 4 schematically illustrates the region of thickened crust constrained to the Romanzof Uplift, away from current seismic activity and located just onshore of the Beaufort fold-and-thrust belt. Based on these results, we suggest that, in contrast to predominant thin-skin deformation across the offshore fold-and-thrust belt, locally thickened crust ($\sim$ 50 km depth Moho) beneath the RUA is likely the result of shortening and stacking of weak igneous and sedimentary rocks since Late Cretaceous (Lane, 2002). In a scenario where deformation is accommodated onshore, the RUA may therefore reflect local aseismic thickening driven by crustal strength variations due to changes in rock composition and rheology. This model does not necessarily require a subduction initiation mechanism.

6 Conclusion

The BSCM has undergone slow deformation from late Cretaceous to the Cenozoic (Lane, 1998). North-south compression may be accommodated by aseismic deformation due to slow deformation and, perhaps, infrequent large earthquakes. Here, we investigate the nature of the BSCM of northern Yukon. The P- and S-wave velocity models reveal an anomalously low-velocity region with V_P/V_S values of 1.7 - 1.78 within the crust beneath the Arctic coast of northern Yukon, indicative of a bulk felsic composition. P- and S-wave velocities in the surrounding regions correspond to a mafic composition at mid crustal depths. This suggests that deformation is controlled by lateral variations in crustal strength attributed to crustal compositions throughout the region. Furthermore, we show that crustal thickening (*i.e.,* thick-skinned deformation) occurs locally beneath the eastern part of the Romanzof Uplift of northern Yukon (Figure 4). The observation of the thickened crust and lack of seismicity in the RUA suggest that deformation could be accommodated aseismically across the narrow margin or more broadly offshore. Neither interpretation would need to evoke the subduction initiation mechanism.

Acknowledgments

We acknowledge financial support from the Natural Science and Engineering Research Council of Canada (Discovery Grants to PA and YL), the Canadian Foundation for Innovation (Canada), and the McGill Department of Earth and Planetary Sciences Wares Postdoctoral Fellowship to CE. Figures were created using Generic Mapping Tools (Wessel et al., 2013).

7 Open Research

The facilities of IRIS Data Services, and specifically the IRIS Data Management Center, were used for archiving and access to waveforms, related metadata, and/or derived products used in this study. IRIS Data Services are funded through the Seismological Facilities for the Advancement of Geoscience and EarthScope (SAGE) Proposal of the National Science Foundation under Cooperative Agreement EAR-1261681. Data from the TA network were made freely available as part of the EarthScope USArray facility, operated by Incorporated Research Institutions for Seismology (IRIS) and supported by the National Science Foundation, under Cooperative Agreements EAR-1261681. Data are available on the IRIS Earthquake Data Center (https://ds.iris.edu/ds/nodes/dmc). Seismic data set is archived at https://doi.org/10.5281/zenodo.6760372. P- and S-wave arrival time data sets and seismic velocity models presented in this work are publicly available at https://doi.org/10.5281/zenodo.6403182.

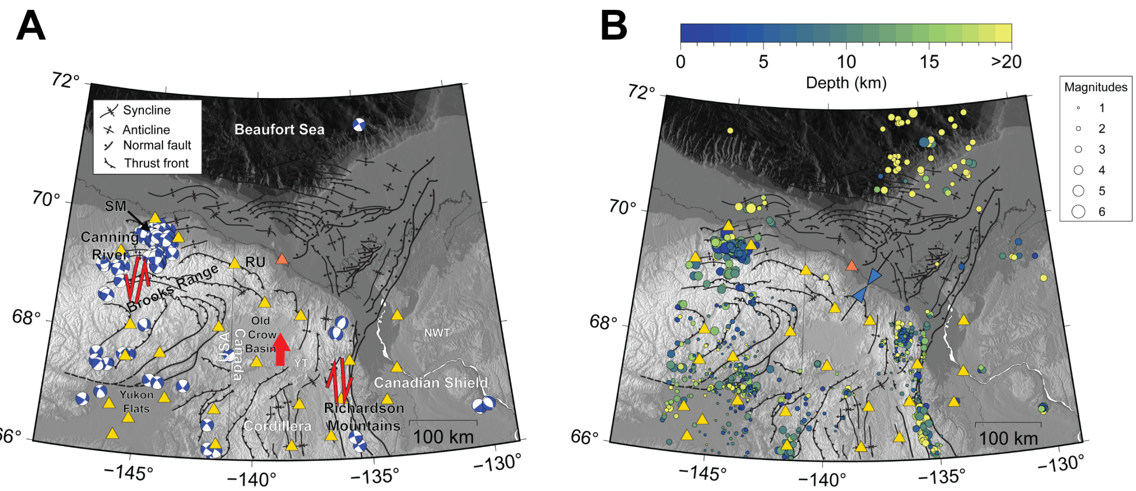

Figure 1. (A) Topographic map showing the main tectonic structures in northeastern Alaska and northwestern Canada (Lane, 2002). Double red arrows indicate styles of current deformation. Single red arrow shows northward residual motion. Focal mechanisms for events ($M \geq 3$) over a time period from November 2012 to August 2021 are shown in blue (Lentas et al., 2019). (B) Events from November 2012 to August 2021 considered in this study are color-coded by depth. Inward facing blue arrows show the average maximum horizontal compressive stress (Heidbach et al., 2018). Seismic stations used in this study are shown as gold triangles. The orange triangle shows the location of the seismic station TA.D28M. Abbreviations: NWT, Northwest Territories; SM, Sadlerochit Mountains; RU, Romanzof uplift; YT, Yukon Territory.

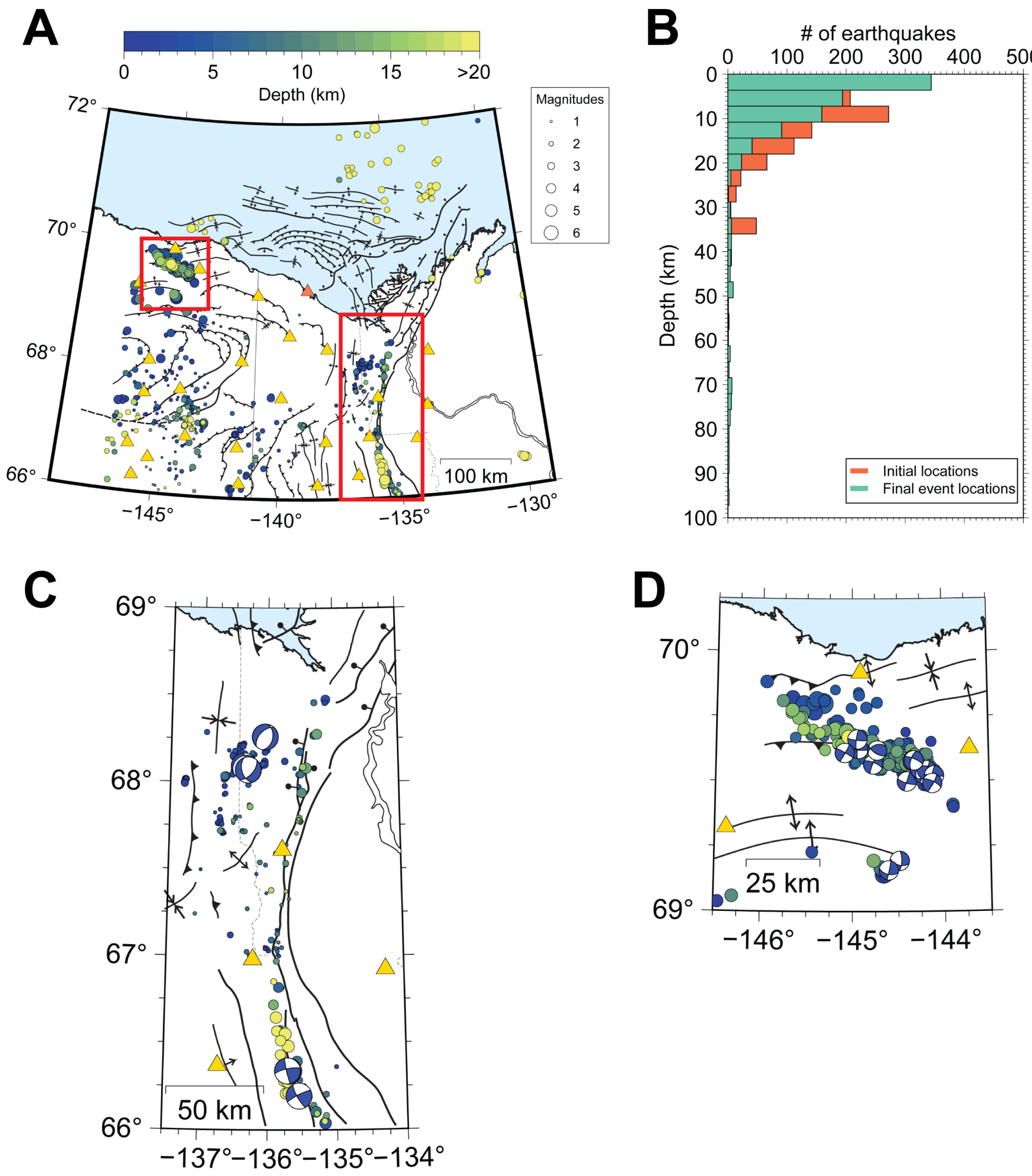

Figure 2. (A) LOTOS relocated seismicity color-coded by depth. Red boxes show locations of zoom-in figures (C and D).(B) 3.6-km-bin histogram showing the depth distribution of initial (orange) and relocated (green) event locations. (C and D) Zoom-in figures around the Richardson Mountains (C) and across northeastern Alaska around the Canning River (D). Tectonic structures are the same as Figure 1.

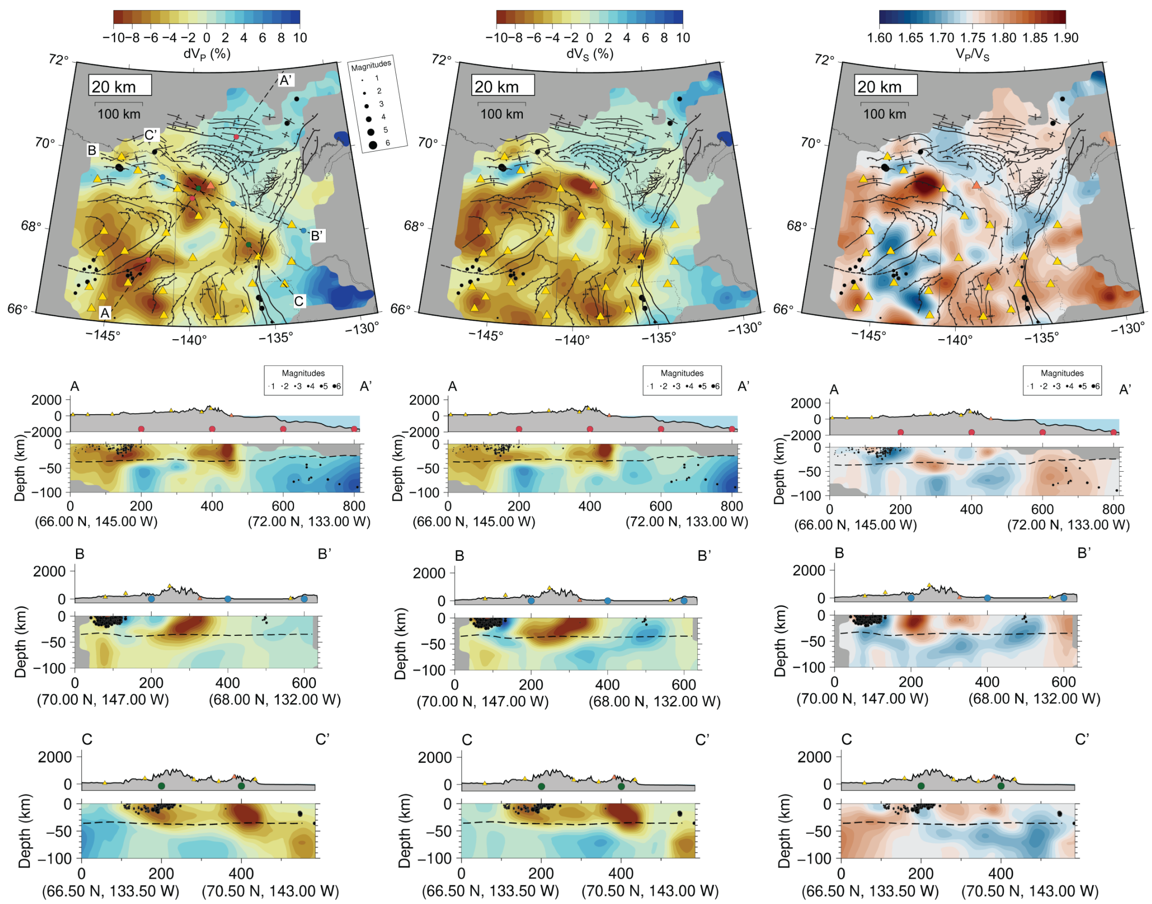

Figure 3. (Top row) 20-km depth slice through the P-wave, S-wave and V_P/V_S models. Transect locations are shown on the 20-km P-wave depth slice. (Middle and bottom rows) Transects A-A', B-B' and CC' through the P-wave, S-wave and V_P/V_S models. Black dashed line shows Moho depth estimates along transect from (Estève et al., 2021). Relocated seismicity within 3 km from depth 20 km are plotted in the top row; within 40 km from each transect are plotted in the middle and bottom rows.

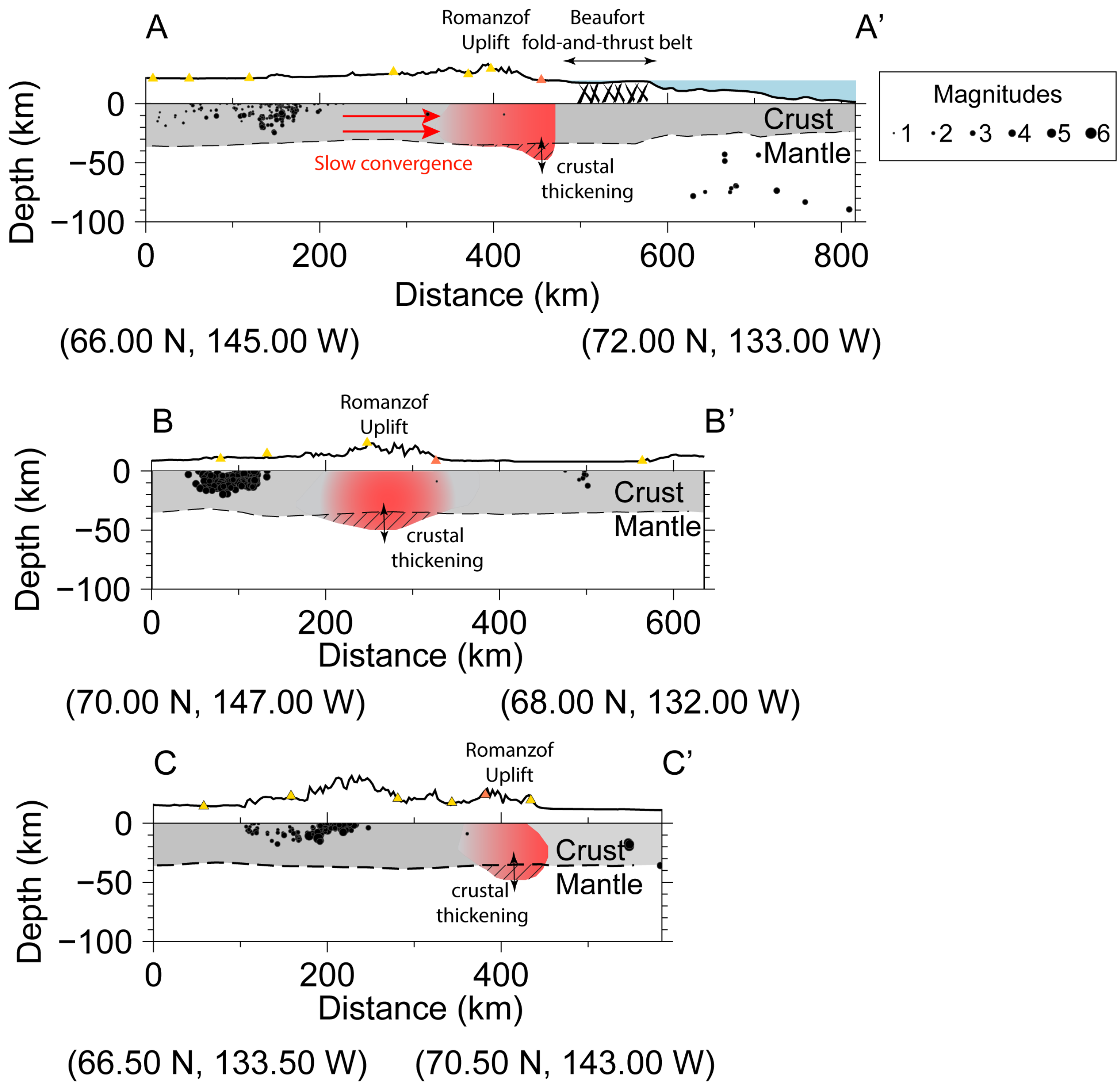

Figure 4. Schematic model depicting the slow deformation occurring at the Beaufort Sea continental margin along transects AA', BB' and CC'. Black dots and triangles depict relocated earthquakes and seismic stations, respectively. The grey shaded area represents the crustal layer along the transect. The red shaded area outlines the RUA within the crust. The hatched area shows inferred crustal thickening at the Beaufort Sea continental margin. Black dashed line shows Moho depth estimates along transect from (Estève et al., 2021).

References

Audet, P., & Ma, S. (2018). Deep crustal earthquakes in the beaufort sea, western canadian arctic, from teleseismic depth phase analysis. *Seismological Research Letters*, *89*(4), 1379–1384. doi: https://doi.org/10.1785/0220180047

Audet, P., Schutt, D. L., Schaeffer, A. J., Estève, C., Aster, R. C., & Cubley, J. F. (2020). Moho variations across the northern Canadian Cordillera. *Seismological Research Letters*, *91*, 3076–3085. doi: https://doi.org/10.1785/0220200166

Cassidy, J. F., & Bent, A. L. (1993, 06). Source parameters of the 29 May and 5 June, 1940 Richardson Mountains, Yukon Territory, earthquakes. *Bulletin of the Seismological Society of America*, *83*(3), 636-659. doi: https://doi.org/10.1785/BSSA0830030636

Cassidy, J. F., Rogers, G. C., & Ristau, J. (2005). Seismicity in the vicinity of the SNORCLE corridors of the northern Canadian Cordillera. *Canadian Journal of Earth Sciences*, *42*(6), 1137–1148. doi: https://doi.org/10.1139/e04-063

Christensen, N. I. (1996). Poisson's ratio and crustal seismology. *Journal of Geophysical Research B: Solid Earth*, *101*(2), 3139–3156. doi: https://doi.org/10.1029/95jb03446

Christensen, N. I., & Mooney, W. D. (1995). Seismic velocity structure and composition of the continental crust: A global view. *Journal of Geophysical Research: Solid Earth*, *100*(B6), 9761-9788. doi: https://doi.org/10.1029/95JB00259

El Khrepy, S., Koulakov, I., Gerya, T., Al-Arifi, N., Alajmi, M. S., & Qadrouh, A. N. (2021). Transition from continental rifting to oceanic spreading in the northern Red Sea area. *Scientific Reports*, *11*(1), 1–7. doi: https://doi.org/10.1038/s41598-021-84952-w

Estève, C., Audet, P., Schaeffer, A. J., Schutt, D., Aster, R. C., & Cubley, J. (2020). The upper mantle structure of northwestern Canada from teleseismic body wave tomography. *Journal of Geophysical Research: Solid Earth*, *125*, 1–18. doi: https://doi.org/10.1029/2019JB018837

Estève, C., Gosselin, J. M., Audet, P., Schaeffer, A. J., Schutt, D. L., & Aster, R. C. (2021). Surface wave tomography of the northern Canadian Cordillera using earthquake Rayleigh wave group velocities. *Journal of Geophysical Research: Solid Earth*(126), 1–22. doi: https://doi.org/10.1029/2021jb021960

Foix, O., Crawford, W. C., Koulakov, I., Baillard, C., Régnier, M., Pelletier, B., & Garaebiti, E. (2019). The 3-D Velocity Models and Seismicity Highlight Forearc Deformation Due to Subducting Features (Central Vanuatu). *Journal of Geophysical Research: Solid Earth*, *124*(6), 5754–5769. doi: https://doi.org/10.1029/2018JB016861

Gaudreau, E., Nissen, E. K., Bergman, E. A., Benz, H. M., Tan, F., & Karasözen, E. (2019). The August 2018 Kaktovik Earthquakes: Active Tectonics in Northeastern Alaska Revealed With InSAR and Seismology. *Geophysical Research Letters*, *46*(24), 14412–14420. doi: https://doi.org/10.1029/2019GL085651

Hasegawa, H. S., Chou, C. W., & Basham, P. W. (1979). Seismotectonics of the Beaufort Sea. *Canadian Journal of Earth Sciences*, *16*, 816–830.

Heidbach, O., Rajabi, M., Cui, X., Fuchs, K., Müller, B., Reinecker, J., . . . Zoback, M. (2018). The world stress map database release 2016: Crustal stress pattern across scales. *Tectonophysics*, *744*, 484-498. doi: https://doi.org/10.1016/j.tecto.2018.07.007

Hyndman, R. D., Cassidy, J. F., Adams, J., Roegrs, G. C., & Mazzotti, S. (2005). Earthquakes and Seismic Hazard in the Yukon- Beaufort-Mackenzie. *Recorder*, *30*(5), 32–66.

Koulakov, I. (2009). LOTOS code for local earthquake tomographic inversion: Benchmarks for testing tomographic algorithms. *Bulletin of the Seismological Society of America*, *99*(1), 194–214. doi: https://doi.org/10.1785/0120080013

Koulakov, I., & Sobolev, S. V. (2006). Moho depth and three-dimensional P and S structure of the crust and uppermost mantle in the Eastern Mediterranean and Middle East derived from tomographic inversion of local ISC data. *Geophysical Journal International*, *164*(1), 218–235. doi: https://doi.org/10.1111/j.1365-246X.2005.02791.x

Lane, L. S. (1998). Latest Cretaceous-Tertiary tectonic evolution of northern Yukon and adjacent Arctic Alaska. *AAPG Bulletin*, *82*(7), 1353–1371.

Lane, L. S. (2002). Tectonic evolution of the Canadian Beaufort Sea - Mackenzie Delta Region: A brief review. *Recorder*, *27*(2), 49–56.

Lane, L. S. (2007). Devonian-Carboniferous paleogeography and orogenesis, northern Yukon and adjacent Arctic Alaska. *Canadian Journal of Earth Sciences*, *44*, 679–694. doi: https://doi.org/10.1139/E06-131

Lane, L. S., & Dietrich, J. R. (1995). Tertiary structural evolution of the Beaufort Sea - Mackenzie Delta region, Arctic Canada. *Bulletin of Canadian Petroleum Geology*, *43*(3), 293–314.

Lentas, K., Di Giacomo, D., Harris, J., & Storchak, D. A. (2019). The isc bulletin as a comprehensive source of earthquake source mechanisms. *Earth System Science Data*, *11*(2), 565–578. doi:

https://doi.org/10.5194/essd-11-565-2019

Leonard, L. J., Hyndman, R. D., Mazzotti, S., Nykolaishen, L., Schmidt, M., & Hippchen, S. (2007). Current deformation in the northern Canadian Cordillera inferred from GPS measurements. *Journal of Geophysical Research: Solid Earth*, *112*(11), 1–15. doi: https://doi.org/10.1029/2007JB005061

Mazzotti, S., Leonard, L. J., Hyndman, R. D., & Cassidy, J. F. (2008). Tectonics , Dynamics , and Seismic Hazard in the Canada – Alaska Cordillera. *Active Tectonics and Seismic Potential of Alaska*, 297–319.

Medved, I., Polat, G., & Koulakov, I. (2021). Crustal structure of the eastern anatolia region (Turkey) based on seismic tomography. *Geosciences*, *11*(2), 1–12. doi: https://doi.org/10.3390/geosciences11020091

Onwuemeka, J., Liu, Y., & Harrington, R. M. (2021). Crustal Velocity Variations and Constraints on Material Properties in the Charlevoix Seismic Zone, Eastern Canada. *Journal of Geophysical Research: Solid Earth*, *126*(7), 1–24. doi: https://doi.org/10.1029/2020JB020918

Paige, C. C., & Saunders, M. A. (1982, mar). Lsqr: An algorithm for sparse linear equations and sparse least squares. *ACM Trans. Math. Softw.*, *8*(1), 43–71. doi: https://doi.org/10.1145/355984.355989

Saltus, R. W., & Hudson, T. L. (2007). Regional magnetic anomalies , crustal strength , and the location of the northern Cordilleran fold-and-thrust belt. *The Geological Society of America*, *35*(6), 567–570. doi: https://doi.org/10.1130/G23470A.1

Talebi, A., Koulakov, I., Moradi, A., Rahimi, H., & Gerya, T. (2020). Ongoing formation of felsic lower crustal channel by relamination in Zagros collision zone revealed from regional tomography. *Scientific Reports*, *10*(1), 1–7. doi: https://doi.org/10.1038/s41598-020-64946-w

Um, J., & Thurber, C. (1987). A fast algorithm for two-point seismic ray tracing. *Bulletin of the Seismological Society of America*, *77*(3), 972-986. doi: https://doi.org/10.1785/BSSA0770030972

van der Sluis, A., & van der Vorst, H. A. (1987). Numerical solution of large, sparse linear algebraic systems arising from tomographic problems. In G. Nolet (Ed.), *Seismic tomography: With applications in global seismology and exploration geophysics* (pp. 49–83). Dordrecht: Springer Netherlands. doi: https://doi.org/10.1007/978-94-009-3899-1_3

Wessel, P., Smith, W. H. F., Scharroo, R., Luis, J., & Wobbe, F. (2013). Generic mapping tools: Improved version released. *Eos*, *94*(45), 409–410. doi: https://doi.org/10.1002/2013EO450001

Wilks, K. R., & Carter, N. L. (1990). Rheology of some continental lower crustal rocks. *Tectonophysics*, *182*(1-2), 57–77. doi: https://doi.org/10.1016/0040-1951(90)90342-6